Journal of Solid State Chemistry 243 (2016) 304–311

Contents lists available at ScienceDirect

Journal of Solid State Chemistry

journal homepage: www.elsevier.com/locate/jssc

Structural chemistry and magnetic properties of the perovskite $SrLa_2Ni_2TeO_9$

Robert Paria Sena [a], Joke Hadermann [a], Chun-Mann Chin [b], Emily C. Hunter [b], Peter D. Battle [b,*]

[a] EMAT, University of Antwerp, Groenenborgerlaan 171, 2020 Antwerp, Belgium
[b] Inorganic Chemistry Laboratory, University of Oxford, South Parks Road, Oxford OX1 3QR, UK

ARTICLE INFO

Article history:
Received 7 July 2016
Received in revised form
31 August 2016
Accepted 1 September 2016
Available online 3 September 2016

Keywords:
Perovskite
Magnetism
Neutron diffraction
Electron microscopy

ABSTRACT

A polycrystalline sample of $SrLa_2Ni_2TeO_9$ has been synthesized using a standard ceramic method and characterized by neutron diffraction, magnetometry and electron microscopy.

The compound adopts a monoclinic, perovskite-like structure with space group $P2_1/n$ and unit cell parameters $a=5.6008(1)$, $b=5.5872(1)$, $c=7.9018(2)$ Å, $\beta=90.021(6)°$ at room temperature. The two crystallographically-distinct B sites are occupied by Ni^{2+} and Te^{6+} in ratios of 83:17 and 50:50.

Both ac and dc magnetometry suggest that the compound is a spin glass below 35 K but the neutron diffraction data show that some regions of the sample are antiferromagnetic. Electron microscopy revealed twinning on a nanoscale and local variations in composition. These defects are thought to be responsible for the presence of two distinct types of antiferromagnetic ordering.

1. Introduction

The chemical flexibility of the perovskite structure is well-established. The basic formulation ABO_3, where A is usually a relatively-large divalent or trivalent cation and B is a smaller cation from the d block or p block, must often be changed to $(A_{2-x}A'_x)BB'O_6$ or $(A_{3-x}A'_x)B_2B'O_9$ to show the presence of more than one type of cation on either the A site or the B site, or both. When the A sites, 12-coordinate in the aristotype cubic structure, are occupied by more than one type of cation, the different cations, A and A', are usually distributed in a disordered manner. However, when the six-coordinate B sites are occupied by multiple cation species the different cations, B and B', often occupy the octahedral sites in an ordered manner [1–3]. The degree of ordering is largely determined by the difference in size and charge of the two cations and it in turn often determines the properties of the compound. For example, Sr_2FeTaO_6 has a disordered distribution of Fe^{3+} and Ta^{5+} over the B sites and behaves as a spin glass below 23 K [4], whereas Sr_2FeIrO_6 has nearly complete 1:1 checkerboard ordering of Fe^{3+} and Ir^{5+} (see Fig. 1) and orders antiferromagnetically at 120 K [5]. This is not the only type of cation ordering observed, but it is the most common. Perhaps surprisingly, it is even found in compounds where it is apparently incompatible with the concentration ratio of the two species, for example $La_3Ni_2SbO_9$ [6]. In this case one set of sites in the checkerboard is occupied entirely by Ni^{2+} while the other is occupied by a disordered 1:2 distribution of Ni^{2+} and Sb^{5+}. Fig. 2 shows the arrangement of the B-site cations in a (001) sheet. The presence of antiferromagnetic ordering below 275 K in $KNiF_3$ [7] suggests that there will be strong antiferromagnetic coupling between nearest-neighbour Ni^{2+} cations in this non-frustrated array and, because of the 3:1 imbalance between the number of these cations on the spin-up and spin-down sublattices, this might be expected to result in ferrimagnetism. Consistent with this, the magnetisation of $La_3Ni_2SbO_9$ increases markedly on cooling below 105 K and measurements of the magnetisation at 5 K found a value in excess of 1.5 μ_B per formula unit. However, neutron diffraction experiments detected little or no magnetic Bragg scattering at 5 K [6]. In order to account for this apparent contradiction it was proposed that ferrimagnetic domains exist, but that they are too small to give rise to Bragg scattering. Support for this hypothesis was provided by neutron diffraction experiments carried out in an applied field. The field apparently brought different domains into alignment, thus increasing the coherence length of the magnetic order and enhanced Bragg scattering was observed [8]. The presence of small magnetic domains was attributed to variations in the Ni/Sb concentration which might be expected to increase the relative significance of next-nearest-neighbour superexchange interactions and hence disrupt the long-range magnetic structure. Evidence for

* Corresponding author.
E-mail address: peter.battle@chem.ox.ac.uk (P.D. Battle).

http://dx.doi.org/10.1016/j.jssc.2016.09.004

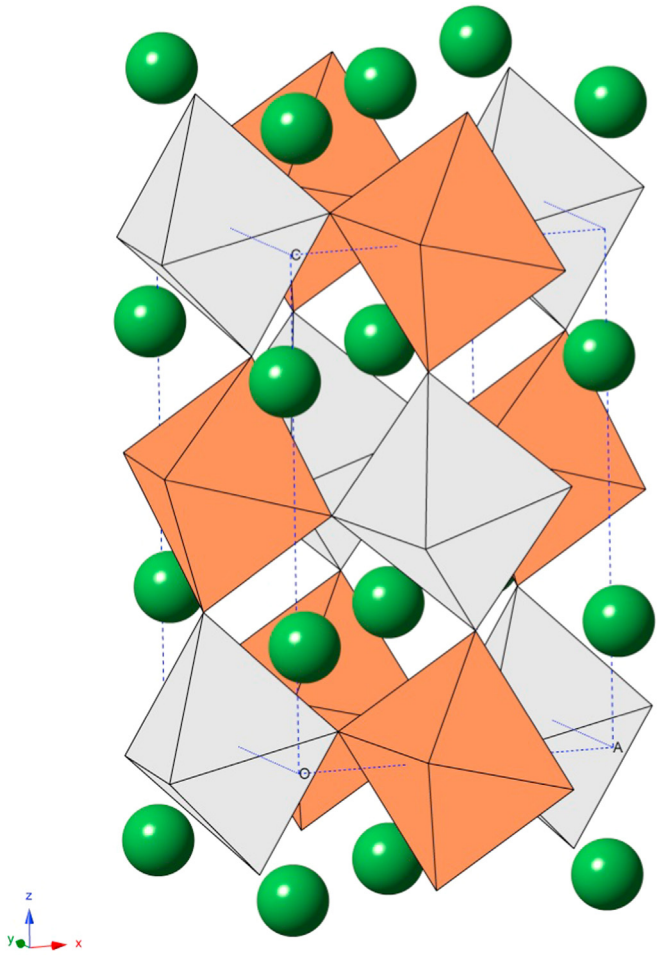

Fig. 1. 1:1 Checkerboard cation ordering in the $A_2BB'O_6$ perovskite structure. Orange and grey octahedra are occupied by B and B' cations, respectively. The A cations are represented by green circles. (For interpretation of the references to color in this figure legend, the reader is referred to the web version of this article.)

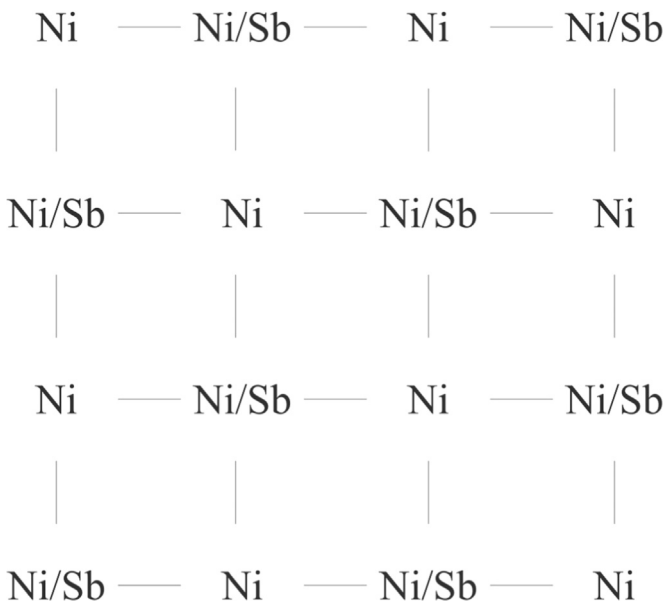

Fig. 2. A 4×4 grid illustrating the cation ordering over the B sites of $La_3Ni_2SbO_9$; one set of sites is occupied by Ni^{2+} only, whereas the other set has a 2:1 concentration ratio of Sb^{5+} and Ni^{2+} (represented by the symbol Ni/Sb).

such variations in the Ni/Sb distribution and the consequent disruption of the cation ordering was provided by high-resolution transmission electron microscopy [8]. Overall, the magnetic behaviour of $La_3Ni_2SbO_9$, that is the enhanced susceptibility associated with local ferrimagnetism but in the absence of long-range order detectable in a diffraction experiment, was deemed to be analogous to the electrical behaviour of relaxor ferroelectrics [9], for example $Pb_3MgNb_2O_9$ [10], and $La_3Ni_2SbO_9$ was consequently described as a relaxor ferromagnet. The formula $(A_{3-x}A'_x)B_2B'O_9$, where B is a paramagnetic cation and B' is diamagnetic, can be satisfied in many different ways and we have therefore begun a program to synthesize more of these oxides in order to identify further examples of relaxor ferromagnetism and to establish the circumstances under which this behaviour occurs. In this paper we describe the synthesis and characterisation of $SrLa_2Ni_2TeO_9$. The two principal differences between this compound and $La_3Ni_2SbO_9$ are that Sb^{5+} has been replaced by the smaller Te^{6+} cation, thus lowering the energy of the valence-shell orbitals of the diamagnetic cation, and that the A sites are now occupied by two cations having different charges. We describe below the consequences of these changes for the magnetic properties of the compound.

2. Experimental

A polycrystalline sample of $SrLa_2Ni_2TeO_9$ was synthesized using the traditional ceramic method. Stoichiometric quantities of $SrCO_3$, NiO, TeO_2 and pre-dried La_2O_3 were initially mixed, ground together and fired in an alumina crucible at 800 °C. The reaction mixture was then pelletised before being heated at 950, 1100, 1200 and finally at 1225 °C, with intermediate regrinding. After a total of six days at 1225 °C the reaction product was cooled to 800 °C in the furnace and then quenched to room temperature.

X-ray powder diffraction data were collected over the angular range $5 \leq 2\theta/^\circ \leq 125$ on a PANalytical Empyrean diffractometer operating with Cu $K_{\alpha 1}$ radiation ($\lambda = 1.54051$ Å) at room temperature. The data were analysed using the Rietveld method [11], as implemented in the GSAS program suite [12], in order to determine the unit cell parameters. Neutron powder diffraction data were collected in angular steps of $\Delta 2\theta = 0.05^\circ$ for $0 \leq 2\theta/^\circ \leq 150$ at room temperature, 50 K and 5 K using the instrument D2b at ILL, Grenoble, France. The sample was held in a vanadium can which was mounted in a Displex refrigerator during the data collection at 5 K. These data were fully analysed using the Rietveld method. A pseudo-Voigt function [13] was employed to model the peak shapes and the background was modelled using an 18-term shifted Chebyshev function. In the analysis of the data collected at room temperature, the unit cell parameters were held at the values determined from the X-ray diffraction data and thus the neutron wavelength was determined to be $\lambda = 1.5937$ Å. Further data sets were collected at temperatures of 5 and 50 K on the diffractometer D1b using a wavelength $\lambda = 2.5238$ Å. D1b has a higher neutron flux than D2b and data from this instrument were used to search for weak Bragg peaks that might go unnoticed on D2b.

Specimens for electron microscopy were prepared by dispersing crushed $SrLa_2Ni_2TeO_9$ powder in ethanol and depositing a few drops of this solution on a copper grid covered with a holey carbon film. Selected-area electron diffraction patterns were recorded with a Philips CM20 transmission electron microscope. High-resolution HAADF–STEM images and atomic resolution STEM-EDX maps were collected with a FEI Titan 80–300 "cubed" transmission electron microscope equipped with a Super-X detector and operated at 300 kV.

The temperature dependence of the dc molar magnetic susceptibility of $SrLa_2Ni_2TeO_9$ was measured using a SQUID magnetometer. Measurements were made while warming the sample

through the temperature range $5 \leq T/K \leq 300$ after it had been cooled in zero field (ZFC) and also after cooling it in the measuring field of 100 Oe (FC). The magnetisation per formula unit (f. u.) was measured as a function of applied magnetic field over the range $-50 \leq H/kOe \leq 50$ at temperatures of 5, 50 and 150 K. The ac susceptibility was measured over the temperature range $2 \leq T/K \leq 150$ in a field of amplitude 3.5 Oe oscillating at frequencies of 1, 10 and 100 Hz.

3. Results

The reaction product was a dark green powder. Our preliminary analysis of the X-ray diffraction pattern suggested that the product consisted principally of a monoclinic, perovskite-like phase contaminated by 1.19(4) wt% of Sr_3TeO_6 and 0.25(3) wt% of NiO. The perovskite pattern could be indexed in space group $P2_1/n$ with $a \sim b \sim \sqrt{2}a_p$, $c \sim 2a_p$, $\beta \sim 90°$ where a_p is the cell parameter of a primitive cubic perovskite. This combination of unit cell size and symmetry allows the presence of two crystallographically-distinct six-coordinate sites in the structure. Our analysis of the X-ray diffraction data suggested that partial cation ordering occurs over the two sites. There was no evidence for the ordering of strontium and lanthanum over the A sites. Fifty crystallites were examined by EDX analysis to rule out the possibility of contamination by Sr_2NiTeO_6 [14]; no La-free crystallites were found. Furthermore, Fourier transforms of the appropriate HRTEM images failed to identify any crystallites with the space group, $I2/m$, associated with Sr_2NiTeO_6.

The temperature dependence of the molar magnetic susceptibility of $SrLa_2Ni_2TeO_9$ is shown in Fig. 3. The data in the temperature range $200 \leq T/K \leq 300$ were fitted to the Curie–Weiss law, resulting in values of 2.21(1) μ_B and +121(2) K for the effective magnetic moment per Ni^{2+} cation and the Weiss constant, respectively. The data collected under ZFC and FC conditions differ below 35 K, at which temperature the former show a maximum in $\chi(T)$; the data collected under FC conditions show essentially no temperature dependence below 35 K. The field dependence of the magnetisation per formula unit is shown in Fig. 4. M(H) is linear at 150 K and nonlinear at 50 K, but no hysteresis is seen at either temperature. However, hysteresis is observed at 5 K. The remanent magnetisation is ~0.06 μ_B per f.u. and the coercive field is 2.4 kOe. The ac susceptibility, see Fig. 5, is a function of frequency and has both real and imaginary components below ~35 K. The transition

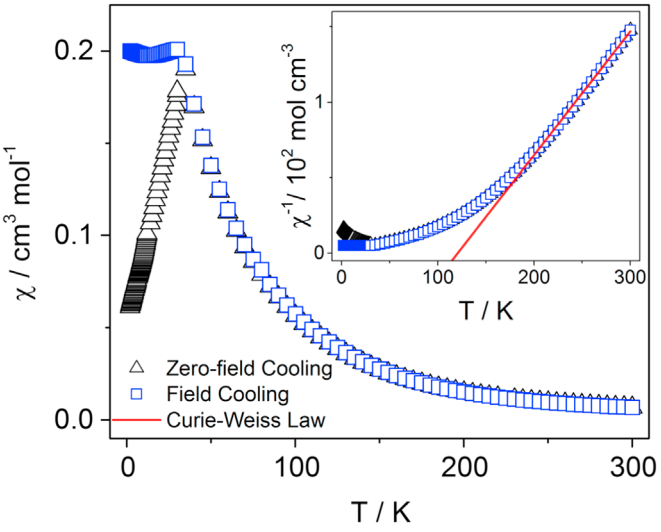

Fig. 3. The molar dc susceptibility and (inset) inverse susceptibility of $SrLa_2Ni_2TeO_9$ as a function of temperature.

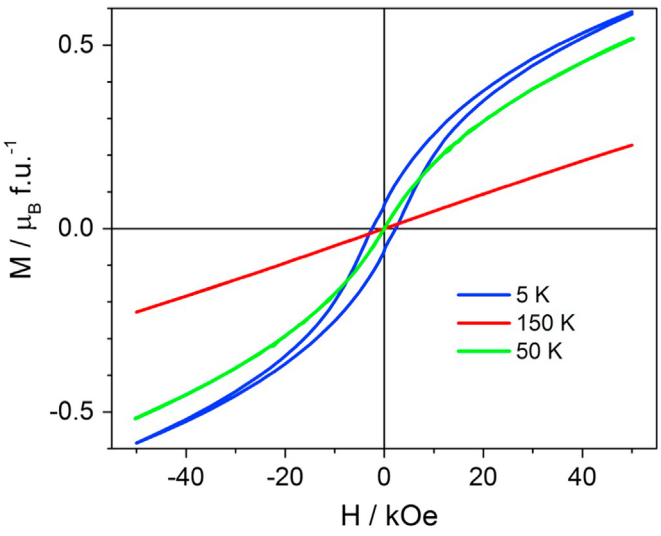

Fig. 4. Magnetic field dependence of the magnetisation per formula unit of $SrLa_2Ni_2TeO_9$ at 5 (blue), 50 (green) and 150 (red) K. (For interpretation of the references to color in this figure legend, the reader is referred to the web version of this article.)

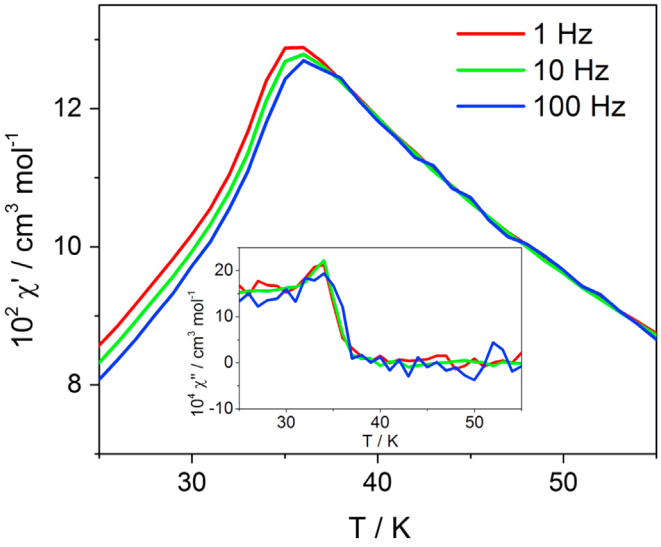

Fig. 5. Temperature and frequency dependence of the real and imaginary components of the ac susceptibility of $SrLa_2Ni_2TeO_9$ collected at 1 (red), 10 (green) and 100 (blue) Hz. (For interpretation of the references to color in this figure legend, the reader is referred to the web version of this article.)

temperature is frequency-dependent with $\Delta T_f/[T_f \Delta(\log \omega)] = 0.014$, a typical value for a canonical spin glass.

Rietveld analysis of the neutron diffraction data collected at room temperature using D2b confirmed that $SrLa_2Ni_2TeO_9$ crystallises in the monoclinic space group $P2_1/n$; ~2.3(3) wt% of Sr_3TeO_6 [15], and ~0.43(3) wt% of unreacted NiO [16] were detected in this analysis. As in the analysis of the X-ray diffraction data, the nickel and tellurium cations were found to be partially ordered over the octahedral sites. The Ni/Te distribution was refined at room temperature and then held constant during the analysis of the data collected at 50 and 5 K. The displacement parameters of the two six-coordinate sites were constrained to be equal during these analyses and the Ni:Te ratio was constrained to be 2:1. The oxygen sublattice was assumed to be fully occupied. The same basic structural model was able to account for all the diffraction patterns. No magnetic Bragg scattering was apparent in any of the datasets collected on D2b. The patterns recorded at room temperature and 5 K are

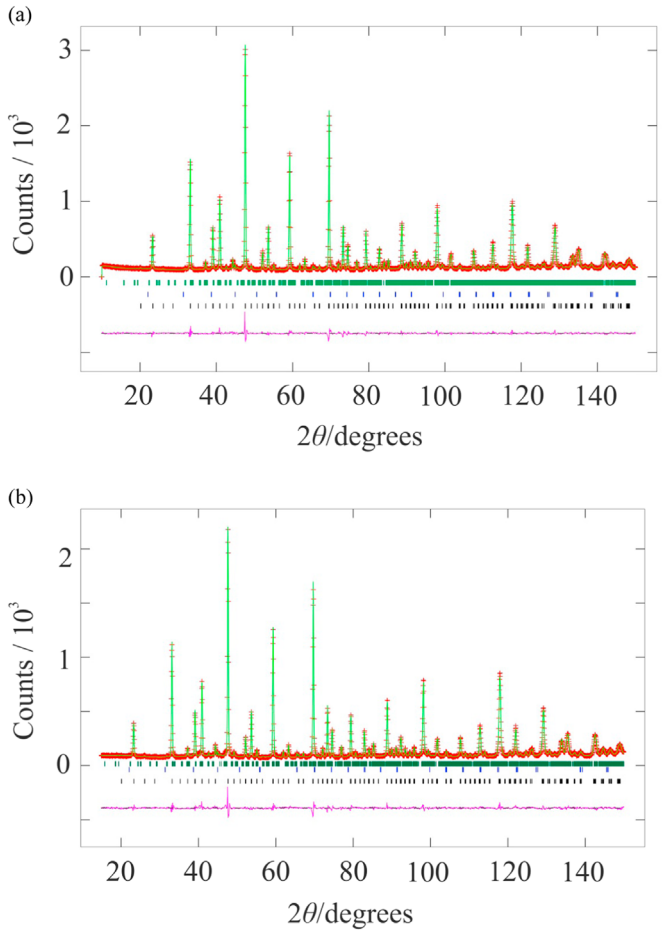

Fig. 6. Observed (red crosses) and calculated (green line) neutron powder diffraction profiles recorded on D2b of $SrLa_2Ni_2TeO_9$ at (a) room temperature and (b) 5 K. Underneath is a difference curve, purple in colour. Reflection markers are shown, from top to bottom, for Sr_3TeO_6, NiO and $SrLa_2Ni_2TeO_9$. (For interpretation of the references to color in this figure legend, the reader is referred to the web version of this article.)

Table 1
Structural parameters of $SrLa_2Ni_2TeO_9$ at room temperature.

Atom	Site	*x*	*y*	*z*	U_{iso}/Å^2	Occupancy
Sr/La	4*e*	0.5050(8)	0.5210(5)	0.2492(20)	0.0275(4)	Sr: 0.3333 La: 0.6667
Ni/Te1	2*c*	0	½	0	0.0026(19)	Ni: 0.83(3) Te: 0.17(3)
Ni/Te2	2*d*	½	0	0	0.0026(19)	Ni: 0.50(3) Te: 0.50(3)
O1	4*e*	0.2322(11)	0.2238(18)	−0.0390(8)	0.0157(20)	1
O2	4*e*	0.2885(11)	0.7212(15)	−0.0309(8)	0.0086(17)	1
O3	4*e*	0.4345(6)	0.9915(7)	0.2480(18)	0.0144(7)	1

R_{wp}=4.87%, R_p=3.68%, χ^2=4.175.
Space group $P2_1/n$: a=5.6008(1) Å, b=5.5872(1) Å, c=7.9018(2) Å, β=90.021(6)°.

presented, along with the calculated patterns, in Fig. 6. The refined structural parameters are presented in Tables 1 and 2 and some selected bond lengths and angles are listed in Tables 3 and 4. The parameters and fits resulting from the analysis of the data collected at 50 K are listed in Tables S1–S3 and Figs. S1 and S2. The neutron diffraction patterns collected at 5 K and 50 K on D1b were superimposable; no additional Bragg scattering was seen at the lower temperature. However, inspection of the data at low angles revealed the presence of a 100 reflection, forbidden in space group $P2_1/n$, and additional intensity in the 101 and 102 reflections of the perovskite

Table 2
Structural parameters of $SrLa_2Ni_2TeO_9$ at 5 K.

Atom	Site	*x*	*Y*	*z*	U_{iso}/Å^2	Occupancy
Sr/La	4*e*	0.5061(8)	0.5237(5)	0.2503(24)	0.0230(4)	Sr: 0.3333 La: 0.6667
Ni/Te1	2*c*	0	½	0	0.0004(2)	Ni: 0.83(3) Te: 0.17(3)
Ni/Te2	2*d*	½	0	0	0.0004(2)	Ni: 0.50(3) Te: 0.50(3)
O1	4*e*	0.2312(12)	0.2200(20)	−0.0345(12)	0.0115(20)	1
O2	4*e*	0.2898(11)	0.7214(18)	−0.0366(12)	0.0052(17)	1
O3	4*e*	0.4325(7)	0.9897(6)	0.2463(16)	0.0095(7)	1

R_{wp}=5.22%, R_p=4.00%, χ^2=3.709.
Space group $P2_1/n$: a=5.5901(1) Å, b=5.5803(1) Å, c=7.8886(2) Å, β=90.026(5)°.

Table 3
Selected bond lengths (Å) in $SrLa_2Ni_2TeO_9$ at room temperature and 5 K.

	Room temperature	5 K
Sr/La–O1	2.880(13)	2.826(17)
Sr/La–O1	2.638(11)	2.665(15)
Sr/La–O1	2.508(11)	2.513(14)
Sr/La–O2	2.760(13)	2.793(17)
Sr/La–O2	2.479(11)	2.453(15)
Sr/La–O2	2.759(11)	2.713(14)
Sr/La–O3	2.984(4)	3.009(4)
Sr/La–O3	2.659(4)	2.633(4)
Sr/La–O3	2.467(6)	2.460(6)
Ni/Te1–O1	2.041(8) × 2	2.046(8) × 2
Ni/Te1–O2	2.049(6) × 2	2.058(7) × 2
Ni/Te1–O3	2.025(14) × 2	2.037(12) × 2
Ni/Te2–O1	1.977(7) × 2	1.959(8) × 2
Ni/Te2–O2	1.972(7) × 2	1.970(7) × 2
Ni/Te2–O3	1.994(14) × 2	1.980(12) × 2

Table 4
Selected bond angles (deg.) in at room temperature and 5 K.

$SrLa_2Ni_2TeO_9$	Room temperature	5 K
O1–Ni/Te1–O2	86.3(5) × 2	86.7(5) × 2
O1–Ni/Te1–O3	89.1(2) × 2	89.6(3) × 2
O2–Ni/Te1–O3	89.4(2) × 2	89.5(3) × 2
O1–Ni/Te2–O2	88.6(5) × 2	89.0(6) × 2
O1–Ni/Te2–O3	88.4(2) × 2	89.5(3) × 2
O2–Ni/Te2–O3	89.6(2) × 2	89.6(3) × 2
Ni/Te1–O1–Ni/Te2	159.7(4)	160.8(5)
Ni/Te1–O2–Ni/Te2	159.3(4)	157.4(5)
Ni/Te1–O3–Ni/Te2	158.8(2)	158.1(2)

phase; the strongest magnetic reflection of nickel oxide was also visible [16,17]. These reflections, which were apparently too weak to be identified in the data collected on D2b, were not seen in the X-ray diffraction pattern at room temperature. They were therefore assumed to be magnetic in origin. None of the collinear antiferromagnetic ordering patterns associated with the perovskite structure gives rise to this combination of reflections [18]. In order to fit the data quantitatively it was therefore assumed that two magnetic phases were present, one showing G-type ordering and the other C-type, see Fig. 7 [18]. In the former, Ni^{2+} cations couple *anti*ferromagnetically to their six nearest-neighbours (NN) whereas in the latter they couple antiferromagnetically to four NN in the (001) sheets but ferromagnetically to the two NN along [001]. The coupling to the twelve next-nearest neighbours (NNN) is entirely ferromagnetic in the G-type structure whereas in the C-type structure there are 4 and 8 ferromagnetic and antiferromagnetic links, respectively. As a consequence of correlations between the parameters, it was not possible to refine the ordered magnetic

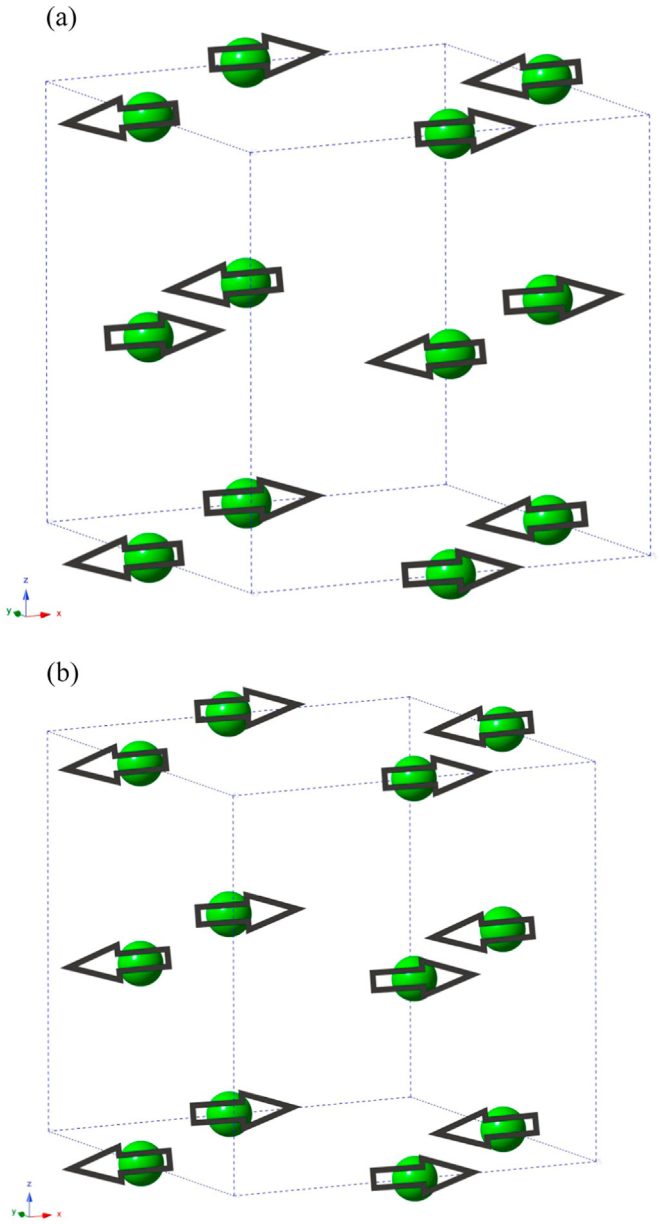

Fig. 7. (a) G-type and (b) C-type magnetic structures drawn in the unit cell of $SrLa_2Ni_2TeO_9$.

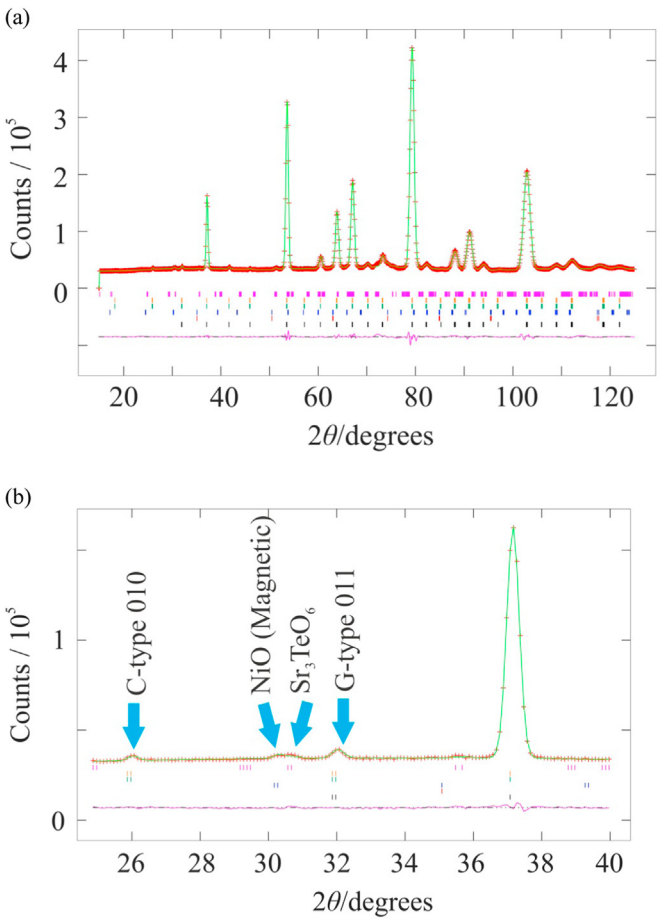

Fig. 8. Observed (red crosses), calculated (green line) and difference (purple line) neutron powder diffraction profiles of $SrLa_2Ni_2TeO_9$ at 5 K recorded on D1b across (a) the full measured angular range and (b) the low–angle region. Reflection markers are shown from top to bottom for Sr_3TeO_6, C-type magnetic $SrLa_2Ni_2TeO_9$, G-type magnetic $SrLa_2Ni_2TeO_9$, magnetic NiO, structural NiO and structural $SrLa_2Ni_2TeO_9$. (For interpretation of the references to color in this figure legend, the reader is referred to the web version of this article.)

moment and the phase fractions of the magnetic phases simultaneously. We therefore assumed that in these two magnetic phases all the 2*c* and 2*d* sites are occupied by Ni^{2+}, and that the magnetic moment is aligned along [100] with a magnitude of 2 μ_B. Refinements, see Fig. 8, then showed that at 5 K 17(2) and 19(2) wt% of the sample ordered as G-type and C-type antiferromagnets, respectively. The limitations of these assumptions are discussed below.

Transmission electron microscopy was applied to check for structural differences on a local scale. The electron diffraction analysis, of which the main zones are shown in Fig. 9, confirms the unit cell and space group derived from X-ray diffraction. More details are given in the electronic supporting information that accompanies this manuscript. The *00l: l≠2 n* reflections are present in [100], but are due to double diffraction, as can be seen by their absence on both the [010] pattern and on the [100] Fourier transform in Fig. 10. Fig. 10 shows a typical crystal along the [100] zone twinned with a [010] zone. The difference between the two orientations is almost imperceptible on the images, but is clear on the Fourier transforms (the Fourier transform for [010] is taken of a smaller area that of [100] because there is no larger domain available; this should not influence the positions and presence of reflections). In the images, the A (La, Sr) columns form a straight line in [010] but a barely-noticeable zig-zag in [100]. In the Fourier transforms, extra reflections are present in [100] compared to [010], corresponding respectively to the reflection conditions *h0l: h+l=2n* and *0kl*: *no conditions*. This twinning is frequent throughout the sample. Note that the reflections *0kl: k=2n+1*, *k+l=2n+1* are present on the electron diffraction patterns of [100], consistent with space group $P2_1/n$, while they are absent on the Fourier transform of [100]. This is a consequence of the fact that the brightness of the dots on HAADF-STEM images increases with the average Z of the projected columns. Consequently, on the HAADF-STEM image the dots of the purely oxygen columns are invisible. They therefore also do not contribute to the Fourier transform of the HAADF-STEM image. We have calculated the theoretical diffraction patterns using the model in Table 1, leaving out the oxygen positions, and these reproduce exactly the patterns seen in the Fourier transforms. The calculated patterns are shown in the Supporting information, Fig. S3.

Besides twinning, another type of inhomogeneity within the crystals was found using energy dispersive X-ray (EDX) analysis. First, STEM-EDX was applied at atomic resolution to confirm the Ni–Te order in the sample. This is shown in Fig. 11, where the

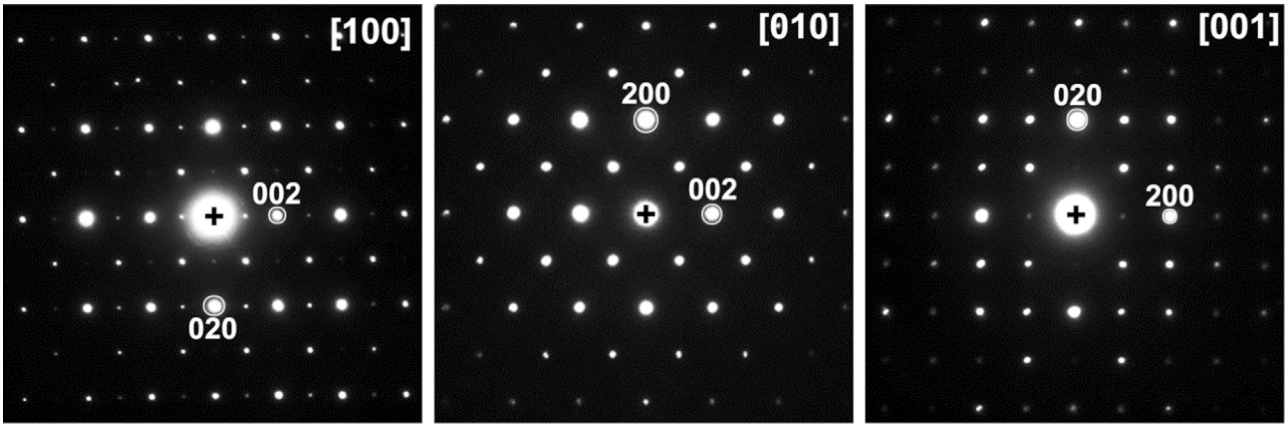

Fig. 9. Representative selected-area electron diffraction patterns for the main zones of $SrLa_2Ni_2TeO_9$.

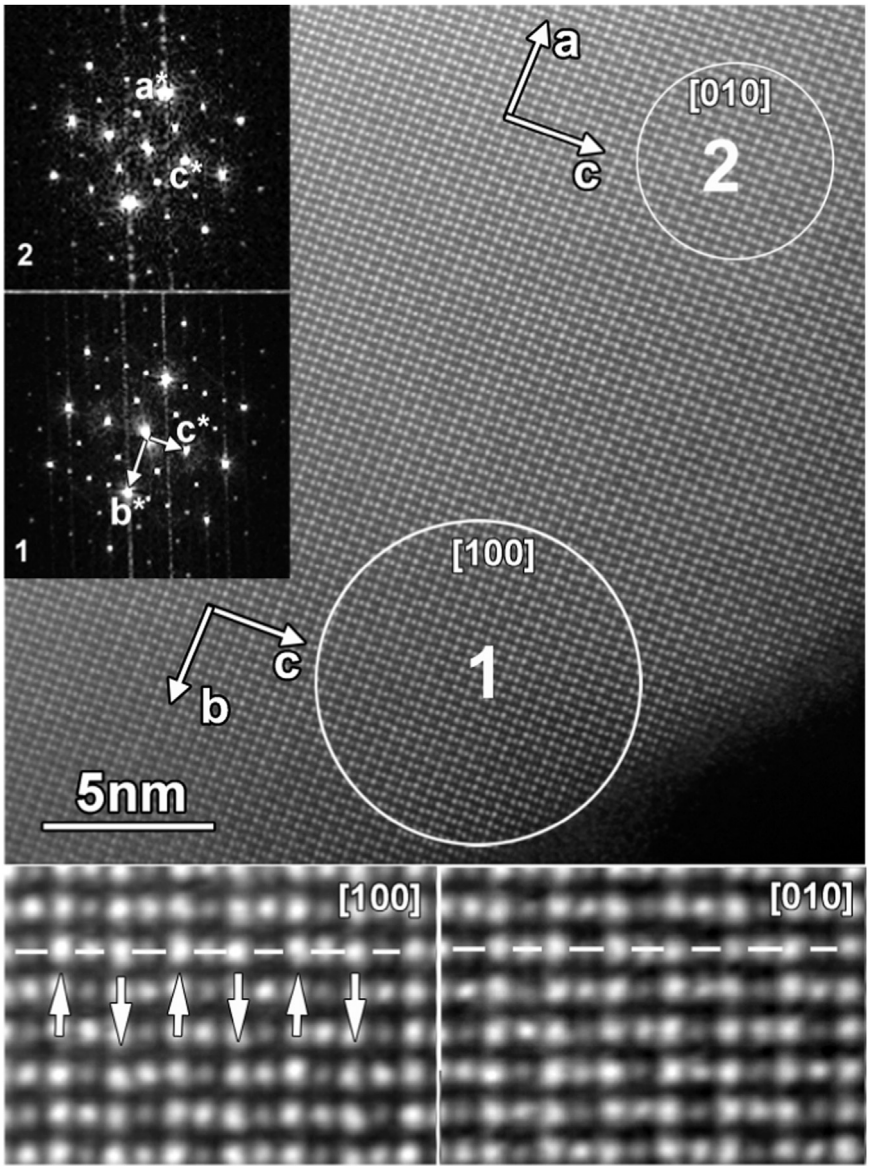

Fig. 10. Aberration-corrected high-resolution HAADF–STEM image of a $SrLa_2Ni_2TeO_9$ crystal. The crystal is twinned and shows the [100] zone at the top, but the [010] zone at the bottom, as can be seen from the Fourier transforms. Arrows on the enlargements at the bottom show the slight shifts of the rows of A cations for [100] and the absence of such shifts in [010], a horizontal line is added as a guide to the eye.

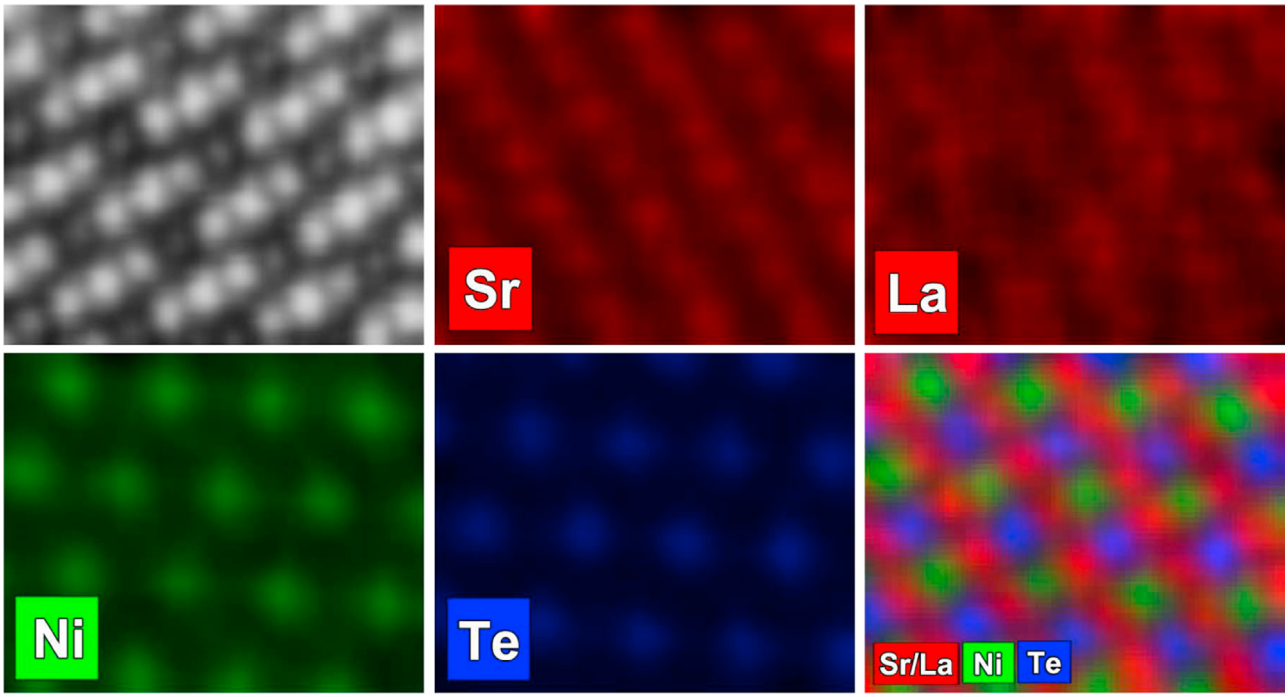

Fig. 11. Aberration-corrected high-resolution HAADF–STEM and STEM-EDX map of a [010] oriented area.

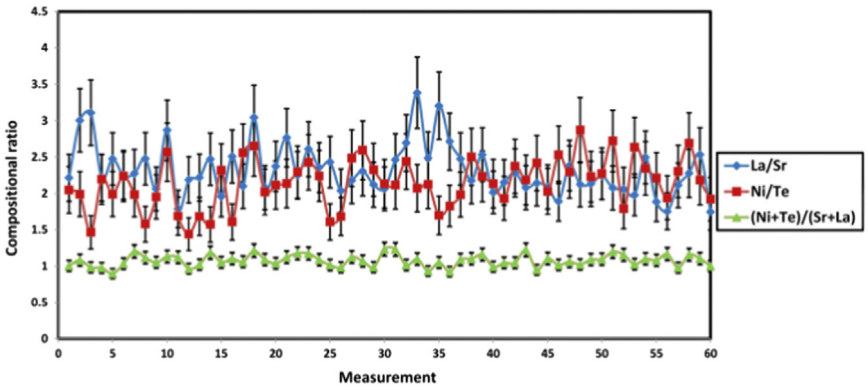

Fig. 12. STEM-EDX measurements on sixty 4.5 nm × 4.5 nm areas within one crystal.

ordered distribution of Ni and Te over the two B cation positions is clearly visible. Next, an overview STEM-EDX analysis was done of several crystals to study the homogeneity of the composition throughout the crystal. In Fig. 12, the results are shown for a representative crystal with a total size of 62 nm by 48 nm. The composition is measured over 60 square areas of 4.5 nm by 4.5 nm, in low magnification. The measurement was performed with the crystal tilted out of zone to avoid channelling effects. Fig. 12 shows the measured ratios between the cations versus the serial number of the measured area. On this graph, the ratio (La+Sr):(Ni+Te) stays close to 1, as required for a perovskite structure. The ratios for the Ni:Te and La:Sr cations, however, deviate significantly from area to area, deviating from the stoichiometric 2:1 ratios for both. When averaging over the whole set of measurements, the composition does agree with the stoichiometric one and is $La_{2.07(9)}Sr_{0.92(9)}Ni_{2.03(13)}Te_{0.97(13)}O_x$ (oxygen values cannot be reliably measured from STEM-EDX quantification on powder samples).

4. Discussion

Our diffraction data demonstrate that there are a number of potentially–important structural differences between $SrLa_2Ni_2TeO_9$ and $La_3Ni_2SbO_9$. The disordered cation distribution over the A sites of the former will result in local static disorder. This is likely to be responsible for the high values of the displacement parameters of the A-site cations and the oxide ions at both room temperature and 5 K, see Tables 1 and 2. The displacement parameters of the anions are also enhanced by the occupational disorder on the B sites. Whereas in $La_3Ni_2SbO_9$ one of the B sites was found, within experimental error, to be totally occupied by Ni^{2+} there is a significant deviation from this ideal ordering pattern in $SrLa_2Ni_2TeO_9$. We shall return to this point below in our discussion of the magnetic properties of the tellurate. The reduced degree of ordering is somewhat surprising given that Ni^{2+} and Te^{6+} differ by more in both size and charge than do Ni^{2+} and Sb^{5+}. The mean bond lengths around the two six coordinate sites are both shorter in the tellurate than in $La_3Ni_2SbO_9$ [6], which is consistent with the presence of some Te^{6+} on the six-coordinate site predominantly occupied by Ni^{2+}, see Table 2.

At first sight, our magnetometry data, along with the neutron diffraction data collected on D2b, suggest that $SrLa_2Ni_2TeO_9$ is a spin glass with $T_g=35$ K. The difference in the behaviour of this compound and $La_3Ni_2SbO_9$ cannot be attributed only to the

additional B-site disorder present in the former. Even in the presence of this disorder, the NN superexchange interactions in the structure illustrated in Fig. 2 are not frustrated, although the introduction of Te–O–Te linkages will modify the relative strengths of the interactions present. The frustration necessary for the formation of a spin glass in this structure is only present when NNN neighbour interactions are competitive with NN interactions. More specifically, when 180° Ni–O–Ni interactions between cations ~3.95 Å apart are in competition with Ni–O–O–Ni interactions between cations ~5.6 Å apart; linear, 7.9 Å Ni–O–Te–O–Ni interactions might also play a role. Each of these interactions, when acting alone, leads to the adoption of a different magnetic structure [18] and so it is plausible to argue that when they are in competition a frustrated spin glass will be formed. The Ni–O–Ni interactions will be less dominant in regions where there is a local excess of tellurium. The data in Fig. 12 demonstrate that such regions exist and we therefore suggest that the inhomogeneous composition of the crystallites is partly responsible for the formation of a spin-glass phase. We must also attempt to explain why $LaSr_2Ni_2TeO_9$ is a spin glass whereas $La_3Ni_2SbO_9$ is a relaxor ferromagnet. In the latter, Ni–O–Ni interactions dominate within ferrimagnetic domains, the boundaries of which are thought to be formed by regions in which the 1:1 cation ordering, as illustrated in Fig. 1, is absent. In these regions, which were seen to extend over at least 50 Å [8], NNN interactions will be more competitive. We did not observe any comparable regions in $SrLa_2Ni_2TeO_9$ and we therefore postulate that the difference in the magnetic behaviour of the two compounds stems from the presence of infrequent but extended disordered regions in $La_3Ni_2SbO_9$ and frequent but local tellurium-rich regions in $LaSr_2Ni_2TeO_9$. The high twinning density in the latter might also be a factor. The presence of extended disordered regions in the antimonate but not in the tellurate is consistent with the greater difference in size and charge of Ni^{2+} and Te^{6+}, as discussed above.

In the discussion above we have linked the magnetic behaviour to the complexity of the microstructure of these perovskites. The neutron diffraction data collected on D1b indicate that there is a further level of complexity that we have not yet considered. Weak magnetic Bragg scattering was observed at 5 K and 50 K. Were it not for the glass–like behaviour of the susceptibility, the observation of magnetic ordering at these temperatures would not be surprising in view of the ordering temperatures of other Ni^{2+}–containing perovskites [19–22]. In order to model this scattering we have postulated that some regions of the sample order as either G-type or C-type *anti*ferromagnets. In order to account for this we must assume that local regions exist wherein the cation ordering is sufficiently regular over a large enough distance to ensure the dominance of NN interactions and hence G-type antiferromagnetism. In other regions, a different cation–ordering pattern, favouring NNN interactions, is established. The former is likely to be nickel-rich and the latter tellurium-rich. We are thus proposing that two different types of antiferromagnetic island can exist within the predominantly glass–like crystallites. Further experimental work will be necessary in order to establish the size of these regions, but the fact that the magnetic scattering persists above the temperature of the susceptibility maximum suggests that they are too large to be described as clusters. Martin et al. have previously proposed a related model based on phase separation to account for the behaviour of $Pr_{0.1}Sr_{0.9}MnO_3$ [23]. The presence of antiferromagnetic regions at relatively high temperatures explains why the effective magnetic moment, 2.21 μ_B per Ni^{2+} cation, derived from the Curie–Weiss law is significantly lower than the spin-only value for Ni^{2+}, 2.83 μ_B. In comparable, perovskite-related compounds the effective magnetic moment is usually enhanced by a small second-order orbital contribution to a value in the range 3.0–3.7 μ_B [19–21]. The magnitude of the reduction seen in $SrLa_2Ni_2TeO_9$ is thus consistent with our conclusion, drawn from the neutron diffraction data, that ~36(3) % of the sample is antiferromagnetic at 5 K. We note that the D1b data can also be modelled using a unique, non-collinear magnetic structure in which the *y* and *z* components of the atomic moments order in C-type and G-type patterns, respectively. In this case, again assuming an ordered moment of 2 μ_B per ordered cation, 25 (2) % of the Ni^{2+} cations would be part of the long-range ordered structure. In view of the composition variations described above we believe that the two-phase magnetic model is more likely to provide the correct interpretation of our data.

5. Conclusion

In contrast to $La_3Ni_2SbO_9$, $SrLa_2Ni_2TeO_9$ does not behave as a relaxor ferromagnet. The principal difference in the average structures deduced from neutron diffraction data is that the 1:1 cation ordering over the B and B′ sites is imperfect in the latter compound. However, in order to explain the observed behaviour it is necessary to consider the variations in microstructure between the two compounds. We have developed a plausible model by considering the length scale associated with the cation disorder in each case. However, more experimental work will be required in order to validate this model.

Acknowledgements

We would like to express our gratitude to E. Suard for the assistance she provided during our visit to ILL and to acknowledge financial support from the EPSRC (EP/M018954/1).

Appendix A. Supporting information

Supplementary data associated with this article can be found in the online version at http://dx.doi.org/10.1016/j.jssc.2016.09.004.

References

[1] S. Vasala, M. Karppinen, Prog. Solid State Chem. 43 (2015) 1–36.
[2] M. Anderson, K. Greenwood, G. Taylor, K. Poeppelmeier, Prog. Solid State Chem. 22 (1993) 197–233.
[3] G. King, P.M. Woodward, J. Mater. Chem. 20 (2010) 5785.
[4] E.J. Cussen, J.F. Vente, D. Battle, T.C. Gibb, J. Mater. Chem. 7 (1997) 459–463.
[5] P.D. Battle, G.R. Blake, T.C. Gibb, J.F. Vente, J. Solid State Chem. 145 (1999) 541–548.
[6] P.D. Battle, S.I. Evers, E.C. Hunter, M. Westwood, Inorg. Chem. 52 (2013) 6648–6653.
[7] R.L. Martin, R.S. Nyholm, N.C. Stephenson, Chem. Ind. (1956) 83–85.
[8] P.D. Battle, M. Avdeev, J. Hadermann, J. Solid State Chem. 220 (2014) 163–166.
[9] A.A. Bokov, Z.-G. Ye, J. Mater. Sci. 41 (2006) 31–52.
[10] P.K. Davies, M.A. Akbas, J. Phys. Chem. Solids 61 (2000) 159–166.
[11] H.M. Rietveld, J. Appl. Crystallogr. 2 (1969) 65–71.
[12] A.C. Larson, R.B. Von Dreele, Los Alamos Natl. Lab. Rep. LAUR, 1994, pp. 86–748.
[13] W.I.F. David, J. Appl. Crystallogr. 19 (1986) 63–64.
[14] L. Ortega-San Martín, J.P. Chapman, G. Cuello, J. González-Calbet, M. I. Arriortua, T. Rojo, Z. Anorg. Allg. Chem. 631 (2005) 2127–2130.
[15] B. Stöger, M. Weil, E. Zobetz, Z. Krist. 225 (2010) 125–138.
[16] G.A. Slack, J. Appl. Phys. 31 (1960) 1571–1582.
[17] W.L. Roth, G.A. Slack, J. Appl. Phys. 352 (1960) 10–12.
[18] E.O. Wollan, W.C. Koehler, Phys. Rev. 100 (1955) 545–563.
[19] D. Iwanaga, Y. Inaguma, M. Itoh, Mater. Res. Bull. 35 (2000) 449–457.
[20] S. Nomura, T. Nakagawa, J. Phys. Soc. Jpn. 21 (1966) 1068.
[21] S. Nomura, T. Nakagawa, J. Phys. Soc. Jpn. 21 (1966) 1679–1684.
[22] V. Scatturin, L. Corliss, N. Elliott, J. Hastings, Acta Crystallogr. (1961) 19–26.
[23] C. Martin, A. Maignan, M. Hervieu, B. Raveau, Z. Jirák, M.M. Savosta, A. Kurbakov, V. Trounov, G. André, F. Bourée, Phys. Rev. B – Condens. Matter Mater. Phys. 62 (2000) 6442–6449.